A Finite Element Treatment of the Angular Dependency of the Even-Parity Equation of Radiative Transfer

R. Becker[1]
e-mail: becker@its.uni-karlsruhe.de

R. Koch

H.-J. Bauer

Institut für Thermische Strömungsmaschinen,
Universität Karlsruhe,
Kaiserstraße 12,
76128 Karlsruhe, Germany

M. F. Modest
Department of Mechanical and Nuclear Engineering,
Pennsylvania State University,
University Park, PA 16802

The present article introduces a new method to solve the radiative transfer equation (RTE). First, a finite element discretization of the solid angle dependence is derived, wherein the coefficients of the finite element approximation are functions of the spatial coordinates. The angular basis functions are defined according to finite element principles on subdivisions of the octahedron. In a second step, these spatially dependent coefficients are discretized by spatial finite elements. This approach is very attractive, since it provides a concise derivation for approximations of the angular dependence with an arbitrary number of angular nodes. In addition, the usage of high-order angular basis functions is straightforward. In the current paper, the governing equations are first derived independently of the actual angular approximation. Then, the design principles for the angular mesh are discussed and the parameterization of the piecewise angular basis functions is derived. In the following, the method is applied to one-dimensional and two-dimensional test cases, which are commonly used for the validation of approximation methods of the RTE. The results reveal that the proposed method is a promising alternative to the well-established practices like the discrete ordinates method (DOM) and provides highly accurate approximations. A test case, which is known to exhibit the ray effect in the DOM, verifies the ability of the new method to avoid ray effects.
[DOI: 10.1115/1.4000233]

1 Introduction

During the last century numerous approximation methods for the calculation of radiation heat transfer were proposed. Acceptable numerical methods are accurate, easy to apply to complex geometries, and have the ability to deal with real radiation problems. Furthermore, the calculation methods should be computationally efficient in terms of memory usage and processing time. Extensive overviews of available methods are given by Viskanta and Mengüc [1], Mishra and Prasad [2] and recently by Viskanta [3].

Virtually all of the generally applicable methods are based on the solution of the radiative transfer equation (RTE), a first-order integrodifferential equation. These solution methods need to account for the spatial and the angular dependence of the radiative intensity. Regarding the angular dependence, the discrete ordinates method (DOM) [4] and the spherical harmonics (P_N) approximation [5] have attracted great attention.

In the DOM the governing equations are easy to derive, the extension to high- order angular approximations is straightforward, and it may be readily applied to complex geometries. Because of these advantages, the DOM has evolved as a standard solution method of the RTE. However, the DOM has several shortcomings, perhaps the most important one being the "ray effect" [6]: In cases with strongly confined radiation sources the integral quantities of radiation transport, e.g., the radiative heat flux, are over- and underestimated for distinct directions. The DOM solves the RTE for a set of discrete directions and the integral quantities are calculated by a weighted sum (quadrature) of the distinct solutions afterwards. This approach is the origin of the ray effect. The usage of higher order quadratures may mask it, but one must be aware that ray effects are inherent to the DOM and also to the derived methods like the finite volume method [7,8]. As a remedy for mitigating the ray effect the modified discrete ordinate method [9] was proposed. However, this method has significant restrictions regarding its general applicability.

In the P_N-approximation the angular dependence of the radiation intensity is expanded into a series of associated Legendre polynomials [10]. Mostly, the series is truncated to the P_1-approximation, seldom a P_3-approximation is used. The origin of this restriction is the serious deficiency of the P_N-approximations: The formulation of the boundary conditions is not straightforward and is tedious for general geometries and high-order approximations. Recently, Modest and Yang [11] published a concise derivation of the equations and the related boundary conditions for high-order P_N-approximations. This may stimulate the usage of P_3 and higher approximations in the future, but the mathematical formulation is still demanding.

These observations have led us to the development of an alternative treatment of the angular dependence in the RTE. Starting out from the second-order even-parity (EP) equation [12] of radiative transport, we derived a finite element discretization of the angular and the spatial domain. This approach enables a continuous representation of the angular dependence of the radiative intensity and hence eliminates ray effects rigorously. Since the mathematical formulation is independent in the selection of the basis functions used for the spatial and the angular finite elements, the extension of the method to high-order approximations is straightforward. This approach has evolved in the early days in the context of the neutron transport equation [13,14], but has received only little attention in the heat transfer community. The authors have adopted the method for solving the radiative heat transfer (RHT) equation as recently proposed by Becker et al. [15]. Comparable methods were lately published by Coelho [16], Pontaza and Reddy [17], Cui and Li [18], and Widmer and Hiptmair [19].

[1]Corresponding author.

Contributed by the Heat Transfer Division of ASME for publication in the JOURNAL OF HEAT TRANSFER. Manuscript received November 13, 2008; final manuscript received March 31, 2009; published online December 4, 2009. Assoc. Editor: Yogesh Jaluria.

2 Derivation of the Equations

2.1 Radiative Transfer Equation. Considering an arbitrary volume V filled with a gray emitting-absorbing, isotropically scattering media, the balance of radiative intensity $I(\mathbf{r},\mathbf{s})$ along a direction $\mathbf{s}$ is given by the radiative transfer equation

$$\mathbf{s}\cdot\nabla I(\mathbf{r},\mathbf{s}) = \kappa I_b(\mathbf{r}) - \beta I(\mathbf{r},\mathbf{s}) + \frac{\sigma}{4\pi}\int_{4\pi} I(\mathbf{r},\mathbf{s}')d\Omega' \tag{1}$$

where α, β, and σ indicate the absorption, the extinction, and the scattering coefficient. I_b is the blackbody intensity, which is related to the temperature T of the medium by

$$I_b = \frac{E_b}{\pi} = \frac{\sigma}{\pi}T^4 \tag{2}$$

If the boundary A of the enclosure is assumed as black and nonreflecting, the intensity $I(\mathbf{r},\mathbf{s})$ at the boundary is

$$I(\mathbf{r}_{\text{wall}},\mathbf{s}) = I_b, \quad \mathbf{n}\cdot\mathbf{s} > 0 \tag{3}$$

for all outward directions $\mathbf{s}$. Equation (1) together with Eq. (3) constitutes a first-order initial value problem. Since this first-order equation is of the hyperbolic type, the stability and the accuracy of the numerical method may be critical and the numerical solution procedure requires provisions like the marching technique. In the current work the problem, as defined by Eqs. (1) and (3), is converted into an equivalent second-order boundary value problem of the parabolic type. This transformation is done by the EP formulation of radiative transfer, which was derived in context of the neutron transport equation [20] and was adopted to the RTE by Song and Park [12].

2.2 Even-Parity Formulation. In the EP formulation the radiative intensity $I(\mathbf{r},\mathbf{s})$ is expressed as a sum of a directional, even-symmetric quantity $\Psi(\mathbf{r},\mathbf{s})$, and a directional, odd-symmetric quantity $\Lambda(\mathbf{r},\mathbf{s})$

$$I(\mathbf{r},\mathbf{s}) = \tfrac{1}{2}[\Psi(\mathbf{r},\mathbf{s}) + \Lambda(\mathbf{r},\mathbf{s})] \tag{4}$$

with

$$\Psi(\mathbf{r},\mathbf{s}) = I(\mathbf{r},\mathbf{s}) + I(\mathbf{r},-\mathbf{s}) \tag{5a}$$

$$\Lambda(\mathbf{r},\mathbf{s}) = I(\mathbf{r},\mathbf{s}) - I(\mathbf{r},-\mathbf{s}) \tag{5b}$$

By using the EP formulation the radiative transfer is fully defined by the calculation of $\Psi(\mathbf{r},\mathbf{s})$ and $\Lambda(\mathbf{r},\mathbf{s})$ in one arbitrary half of the solid angle. This can be easily shown by evaluating the radiative heat flux $q(\mathbf{r})$ and the incident radiation $G(\mathbf{r})$

$$\mathbf{q}(\mathbf{r}) = \int_{4\pi} \mathbf{s} I(\mathbf{r},\mathbf{s})d\Omega \tag{6a}$$

$$G(\mathbf{r}) = \int_{4\pi} I(\mathbf{r},\mathbf{s})d\Omega \tag{6b}$$

Substituting $I(\mathbf{r},\mathbf{s})$ as given by Eq. (4) into Eqs. (6*a*) and (6*b*) and using the symmetry properties of $\Psi(\mathbf{r},\mathbf{s})$ and $\Lambda(\mathbf{r},\mathbf{s})$, the integration in Eqs. (6*a*) and (6*b*) can be restricted to 1/2 of the solid angle

$$\mathbf{q}(\mathbf{r}) = \tfrac{1}{2}\int_{4\pi} \mathbf{s}[\Psi(\mathbf{r},\mathbf{s}) + \Lambda(\mathbf{r},\mathbf{s})]d\Omega = \int_{2\pi} \mathbf{s}\Lambda(\mathbf{r},\mathbf{s})d\Omega \tag{7a}$$

$$G(\mathbf{r}) = \tfrac{1}{2}\int_{4\pi} [\Psi(\mathbf{r},\mathbf{s}) + \Lambda(\mathbf{r},\mathbf{s})]d\Omega = \int_{2\pi} \Psi(\mathbf{r},\mathbf{s})d\Omega \tag{7b}$$

Formulating Eq. (1) for the two directions $\mathbf{s}$ and $-\mathbf{s}$, adding and subtracting the resulting equations and substituting Eqs. (5*a*) and (5*b*), a system of coupled differential equations in $\Psi(\mathbf{r},\mathbf{s})$ and $\Lambda(\mathbf{r},\mathbf{s})$ is obtained

$$\mathbf{s}\cdot\nabla\Lambda(\mathbf{r},\mathbf{s}) + \beta\Psi(\mathbf{r},\mathbf{s}) = 2\kappa I_b(\mathbf{r}) + \frac{\sigma}{2\pi}\int_{2\pi} \Psi(\mathbf{r},\mathbf{s}')d\Omega' \tag{8a}$$

$$\mathbf{s}\cdot\nabla\Psi(\mathbf{r},\mathbf{s}) + \beta\Lambda(\mathbf{r},\mathbf{s}) = 0 \tag{8b}$$

Solving Eq. (8*b*) for the odd quantity $\Lambda(\mathbf{r},\mathbf{s})$

$$\Lambda(\mathbf{r},\mathbf{s}) = -\frac{1}{\beta}\mathbf{s}\cdot\nabla\Psi(\mathbf{r},\mathbf{s}) \tag{9}$$

and inserting Eq. (9) in Eq. (8*a*), the following second-order differential equation

$$-\mathbf{s}\cdot\nabla\frac{1}{\beta}\mathbf{s}\cdot\nabla\Psi(\mathbf{r},\mathbf{s}) + \beta\Psi(\mathbf{r},\mathbf{s}) = 2\kappa I_b(\mathbf{r}) + \frac{\sigma}{2\pi}\int_{2\pi} \Psi(\mathbf{r},\mathbf{s}')d\Omega' \tag{10}$$

of radiative transfer is derived.

Contrary to the initial value problem, as defined in Sec. 2.1, the EP equation needs a boundary condition for the inward and the outward directions. These boundary conditions can be deduced from Eq. (3) by replacing the intensity $I(\mathbf{r},\mathbf{s})$ with Eq. (4) and using the symmetry properties of $\Psi(\mathbf{r},\mathbf{s})$ and $\Lambda(\mathbf{r},\mathbf{s})$. Following this path, the boundary condition

$$\Psi(\mathbf{r},\mathbf{s}) - \text{sign}(\mathbf{n}\cdot\mathbf{s})\frac{1}{\beta}\mathbf{s}\cdot\nabla\Psi(\mathbf{r},\mathbf{s}) = 2I_b(\mathbf{r}) \tag{11}$$

is obtained.

With Eqs. (10) and (11) the radiative transfer is transformed to a second-order differential equation of the parabolic type. The use of this second-order boundary value problem instead of the first-order initial value problem enables one to adopt the standard Galerkin approach, which provides unconditional stability, to solve the RTE.

2.3 Weak Solution. A common procedure for the derivation of the governing equations of the Galerkin finite element method (FEM) is the application of the weighted residual method [21].

In this method the differential equation is multiplied by a weight function $W(\mathbf{r},\mathbf{s})$ and the integrated residual is set to zero. In the traditional approach this integration is restricted to the spatial domain, and the directional dependence is addressed by the DOM [22]. Here, the directional and the spatial dependence are approximated by means of the FEM. Therefore, the integration includes both, the angular and spatial, domains.

The weighted residual approach is written as

$$\int_{2\pi}\int_{V}\left[\mathbf{s}\cdot\nabla\frac{1}{\beta}\mathbf{s}\cdot\nabla\Psi(\mathbf{r},\mathbf{s}) - \beta\Psi(\mathbf{r},\mathbf{s}) + \frac{\sigma}{2\pi}\int_{2\pi}\Psi(\mathbf{r},\mathbf{s}')d\Omega' + 2\kappa I_b(\mathbf{r})\right]W(\mathbf{r},\mathbf{s})dVd\Omega = 0 \tag{12}$$

Using Green's theorem and integrating the second-order derivative by parts, leads to the so-called weak formulation of the EP equation

$$\int_{2\pi}\int_{A}(\mathbf{n}\cdot\mathbf{s})\frac{1}{\beta}\mathbf{s}\cdot\nabla\Psi(\mathbf{r},\mathbf{s})W(\mathbf{r},\mathbf{s})dAd\Omega$$
$$-\int_{2\pi}\int_{V}\frac{1}{\beta}\mathbf{s}\cdot\nabla\Psi(\mathbf{r},\mathbf{s})\mathbf{s}\cdot\nabla W(\mathbf{r},\mathbf{s})dVd\Omega$$
$$-\int_{2\pi}\int_{V}\left[\beta\Psi(\mathbf{r},\mathbf{s})-\frac{\sigma}{2\pi}\int_{2\pi}\Psi(\mathbf{r},\mathbf{s}')d\Omega'\right]W(\mathbf{r},\mathbf{s})dVd\Omega$$
$$+\int_{2\pi}\int_{V}2\kappa I_b(\mathbf{r})W(\mathbf{r},\mathbf{s})dVd\Omega=0 \tag{13}$$

where the integration over the boundary A is used to fulfill the boundary condition Eq. (11). The boundary condition is integrated in Eq. (13) by solving Eq. (11) for

$$\frac{1}{\beta}\mathbf{s}\cdot\nabla\Psi(\mathbf{r},\mathbf{s})=\mathrm{sign}(\mathbf{n}\cdot\mathbf{s})[\Psi(\mathbf{r},\mathbf{s})-2I_b(\mathbf{r})] \tag{14}$$

and replacing the integrand in the area term in Eq. (13). This leads to the integral equation

$$\int_{2\pi}\int_{A}|\mathbf{n}\cdot\mathbf{s}|[\Psi(\mathbf{r},\mathbf{s})-2I_b(\mathbf{r})]W(\mathbf{r},\mathbf{s})dAd\Omega$$
$$-\int_{2\pi}\int_{V}\frac{1}{\beta}\mathbf{s}\cdot\nabla\Psi(\mathbf{r},\mathbf{s})\mathbf{s}\cdot\nabla W(\mathbf{r},\mathbf{s})dVd\Omega$$
$$-\int_{2\pi}\int_{V}\left[\beta\Psi(\mathbf{r},\mathbf{s})-\frac{\sigma}{2\pi}\int_{2\pi}\Psi(\mathbf{r},\mathbf{s}')d\Omega'\right]W(\mathbf{r},\mathbf{s})dVd\Omega$$
$$+\int_{2\pi}\int_{V}2\kappa I_b(\mathbf{r})W(\mathbf{r},\mathbf{s})dVd\Omega=0 \tag{15}$$

which is the starting point for the following finite element discretization.

2.4 Finite Element Formulation. For the discretization of Eq. (15) and the derivation of the algebraic linear system by means of finite elements two formulations are suitable. On the one hand, the equations may be discretized by using elemental basis functions to approximate the solution and the weighting function as a series expansion locally. Afterwards the global system is constructed by superposition of the elemental contributions. This approach is often used, since it is the most convenient for implementing the finite element method in a computer code. On the other hand, the derivation of the algebraic system may be achieved by using globally defined basis functions. For the present purpose it is more advantageous to use the global approach, since it results in a formulation, which is much easier to compare with the DOM or the P_N-approximations. Later on, the separation of the globally defined functions into the elemental contributions will be examined in a brief manner.

By introducing the angular approximation, the EP quantity $\Psi(\mathbf{r},\mathbf{s})$ is written as

$$\Psi(\mathbf{r},\mathbf{s})=\sum_{n}^{M_\Omega}\Psi_n(\mathbf{r})\Phi_n(\mathbf{s}) \tag{16}$$

and the weight function $W(\mathbf{r},\mathbf{s})$ is

$$W(\mathbf{r},\mathbf{s})=\sum_{n}^{M_\Omega}W_n(\mathbf{r})\Phi_n(\mathbf{s}) \tag{17}$$

where the spatial dependence of $\Psi(\mathbf{r},\mathbf{s})$ and $W(\mathbf{r},\mathbf{s})$ is still unknown. Hence, the coefficients $\Psi_n(\mathbf{r})$ and $W_n(\mathbf{r})$ are just spatially dependent coefficients of the angular basis function $\Phi_n(\mathbf{s})$. The choice of suitable angular basis functions is limited by two restrictions: They must be linearly independent and they must also be square integrable over the angular domain. These requirements are fulfilled by every piecewise defined function of any order. Inserting the expansions (16) and (17) into the weighted residual Eq. (15), a system of M_Ω equations

$$\sum_{n}^{M_\Omega}\int_{A}[\Psi_n(\mathbf{r})\bar{\Omega}_{nm}-2I_b(\mathbf{r})\bar{\omega}_m]W_m(\mathbf{r})dA$$
$$-\int_{V}\frac{1}{\beta}\nabla^T\Psi_n(\mathbf{r})\Omega^{11}_{nm}\nabla W_m(\mathbf{r})dV-\int_{V}\beta\Psi_n(\mathbf{r})\Omega^{00}_{nm}W_m(\mathbf{r})dV$$
$$+\int_{V}\left[\frac{\sigma}{2\pi}\Psi_n(\mathbf{r})\omega^{00}_n\omega^{00}_m+2I_b(\mathbf{r})\omega^{00}_m\right]W_m(\mathbf{r})dV=0 \tag{18}$$

with the coefficients

$$\Omega^{11}_{nm}=\int_{2\pi}\begin{pmatrix}\xi\xi & \xi\eta & \xi\mu\\ \eta\xi & \eta\eta & \eta\mu\\ \mu\xi & \mu\eta & \mu\mu\end{pmatrix}\Phi_n(\mathbf{s})\Phi_m(\mathbf{s})d\Omega \tag{19a}$$

$$\Omega^{01}_{nm}=\int_{2\pi}\mathbf{s}\Phi_n(\mathbf{s})\Phi_m(\mathbf{s})d\Omega \tag{19b}$$

$$\Omega^{00}_{nm}=\int_{2\pi}\Phi_n(\mathbf{s})\Phi_m(\mathbf{s})d\Omega \tag{19c}$$

$$\omega^{00}_m=\int_{2\pi}\Phi_m(\mathbf{s})d\Omega \tag{19d}$$

$$\bar{\Omega}_{nm}=\int_{2\pi}|\mathbf{n}\cdot\mathbf{s}|\Phi_n(\mathbf{s})\Phi_m(\mathbf{s})d\Omega \tag{19e}$$

$$\bar{\omega}_m=\int_{2\pi}|\mathbf{n}\cdot\mathbf{s}|\Phi_m(\mathbf{s})d\Omega \tag{19f}$$

is obtained.

Equation (18) constitutes a linear system for the determination of the coefficients $\Psi_n(\mathbf{r})$ in the angular domain, where the spatial dependence is left to later analysis. Clearly, the choice of the basis functions determines the pattern of sparsity in the matrices. If, e.g., piecewise constant, nonoverlapping basis functions are used, all off-diagonal terms in the matrix are zero and a system of equations similar to the one derived by the DOM will be obtained [14]. On the other hand, if high-order polynomials defined in the whole angular domain are chosen, a system of equations comparable to the P_N-approximation will be derived. For the subsequent analysis, piecewise linear basis functions with compact support are applied for the angular approximation and, as a result, all off-diagonal terms marking adjacent nodes are nonzero.

The fully, spatially, and angularly, discretized algebraic equation for the RHT problem, as defined by Eq. (15), is derived by substituting a suitable approximation for the coefficients $\Psi_n(\mathbf{r})$ in Eq. (18). Again, the unknowns are expanded into a series of globally defined basis functions, here in the spatial domain $\hat{\Phi}_p(\mathbf{r})$. With

$$\Psi_n(\mathbf{r})=\sum_{p}^{M_r}\Psi_{np}\hat{\Phi}_p(\mathbf{r}) \tag{20a}$$

$$W_n(\mathbf{r})=\sum_{p}^{M_r}\hat{\Phi}_p(\mathbf{r}) \tag{20b}$$

the approximations of the EP quantity

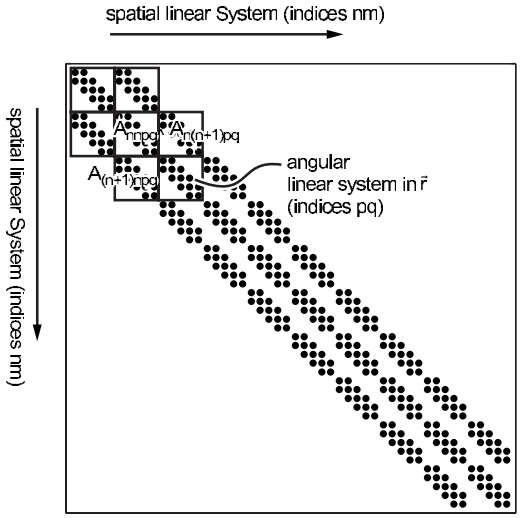

Fig. 1 Structure of the spatial and angular linear system

$$\Psi(\mathbf{r},\mathbf{s}) = \sum_{p}^{M_r} \sum_{n}^{M_\Omega} \Psi_{np} \hat{\Phi}_p(\mathbf{r}) \Phi_n(\mathbf{s}) \tag{21}$$

and the weight function

$$W(\mathbf{r},\mathbf{s}) = \sum_{p}^{M_r} \sum_{n}^{M_\Omega} \hat{\Phi}_p(\mathbf{r}) \Phi_n(\mathbf{s}) \tag{22}$$

are deduced as a product of basis functions for the direction **s** and position **r**. Substituting Eqs. (20*a*) and (20*b*) into Eq. (18), one equation of the resultant linear system in position and direction reads:

$$\sum_{p}^{M_r} \sum_{n}^{M_\Omega} A_{nmpq} \Psi_{mq} = b_{np} \tag{23}$$

with matrix elements

$$A_{nmpq} = \int_A \hat{\Phi}_p(\mathbf{r}) \bar{\Omega}_{nm} \hat{\Phi}_q(\mathbf{r}) dA - \int_V \frac{1}{\beta} \nabla^T \hat{\Phi}_p(\mathbf{r}) \Omega_{nm}^{11} \nabla \hat{\Phi}_q(\mathbf{r}) dV - \int_V \beta \hat{\Phi}_p(\mathbf{r}) \Omega_{nm}^{00} \hat{\Phi}_q(\mathbf{r}) dV + \int_V \frac{\sigma}{2\pi} \hat{\Phi}_p(\mathbf{r}) \omega_n^{00} \omega_m^{00} \hat{\Phi}_q(\mathbf{r}) dV \tag{24}$$

and source term

$$b_{np} = 2 \int_A I_b(\mathbf{r}) \bar{\omega}_n \hat{\Phi}_p(\mathbf{r}) dA - 2 \int_V I_b(\mathbf{r}) \omega_n^{00} \hat{\Phi}_p(\mathbf{r}) dV \tag{25}$$

Equation (23) defines the linear system

$$\mathbf{A}\Psi = \mathbf{b}$$

$$\Psi = (\Psi_{11}, \Psi_{12}, \ldots, \Psi_{1M_\Omega}, \ldots, \Psi_{M_r M_\Omega}) \tag{26}$$

with an underlying block structure where the angular equations Eq. (18) are embedded in the system defined by the spatial approximation (Fig. 1).

With results calculated from the solution of Eq. (26), the incident radiation Eq. (7*b*) is calculated from

$$G(\mathbf{r}) = \sum_{p}^{M_r} \sum_{n}^{M_\Omega} \int_{2\pi} \Phi_n(\mathbf{s}) d\Omega \Phi_p(\mathbf{r}) \Psi_{np} = \sum_{p}^{M_r} \sum_{n}^{M_\Omega} \omega_n^{00}(\mathbf{s}) \Phi_p(\mathbf{r}) \Psi_{np} \tag{27}$$

and the heat flux Eq. (7*a*) is given by

$$\mathbf{q}(\mathbf{r}) = -\frac{1}{\beta} \sum_{p}^{M_r} \sum_{n}^{M_\Omega} \int_{2\pi} \mathbf{s} \otimes \mathbf{s} \Phi_n(\mathbf{s}) d\Omega \nabla \Phi_p(\mathbf{r}) \Psi_{np} = -\frac{1}{\beta} \sum_{p}^{M_r} \sum_{n}^{M_\Omega} \omega_n^{11} \nabla \Phi_p(\mathbf{r}) \Psi_{np} \tag{28}$$

As stated earlier the most convenient way of implementing the finite element method in a computer code is by adding the global coefficients from the elemental contributions. In order to do this, the angular domain Ω and the spatial domain V are decomposed in nonoverlapping elements Ω^e and V^e in such a way that

$$V = \sum_e V^e \tag{29}$$

and

$$\Omega = \sum_e \Omega^e \tag{30}$$

With these subdivisions the global angular and spatial basis functions are split into the elemental parts

$$\hat{\Phi}_p(\mathbf{r}) = \sum_e \hat{\Phi}_p^e(\mathbf{r}) \tag{31a}$$

$$\Phi_n(\mathbf{s}) = \sum_e \Phi_n^e(\mathbf{s}) \tag{31b}$$

and hence the coefficients can be calculated by restricting the integrations to the elements V^e and Ω^e. Afterwards, the elemental coefficients are added according to the continuity requirements as defined by Eqs. (31*a*) and (31*b*).

2.5 Angular Discretization and Definition of the Basis Functions. Up to this point, no assumptions about the nature of the basis functions other than those at the beginning of Sec. 2.4 were made. As stated earlier, piecewise angular functions are used in the subsequent calculations. Consequently, the definition of the basis functions requires two steps: First, the elemental decomposition of the solid angle, and second, the definition of the elemental basis functions on those elements.

To perform the angular decomposition, meshes based on octahedrons were used, even if simpler schemes, e.g., the classical longitudinal/latitudinal subdivisions, are available. The reason for this choice is the symmetry under rotations of $\pi/2$ and the nearly equally sized angular elements of the octahedral meshes. According to the principles for the construction of quadratures for use with the DOM, these attributes are believed to be crucial for the accuracy of numerical results [23].

The angular meshes are constructed in the following way. Starting out from an octahedron inscribed in the unit sphere with the vertices placed on the coordinate axes, the edges of the basic planar triangles are subdivided into N equal parts by $N-1$ new nodes. Afterwards the nodes are connected by lines parallel to the edges of the basic triangles leading to a finer triangular grid. On each intersection of the connecting lines, additional nodes are placed. An example of this triangulation of order $N=2$ is presented in Fig. 2. The spherical grid is built afterwards by projecting the triangulation onto the unit sphere (Fig. 2). Following this procedure, grids with

$$M_\Omega = 6, 18, 38, \ldots, (4N^2 + 2) \tag{32}$$

nodes and $8, 32, 72, \ldots, 8N^2$ elements are obtained.

It should be emphasized that the procedure described here sub-

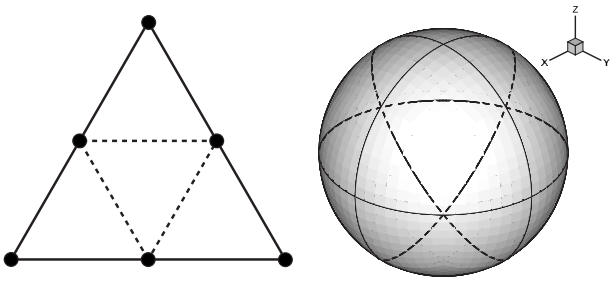

Fig. 2 Triangulation of the order $N=2$ and the derived octahedral angular finite element mesh

divides the whole solid angle, even though the application of the EP formulation requires only the partitioning of one arbitrary half of the solid angle. This reduction to the half angle is readily obtained by splitting the mesh at, e.g., the equatorial plane.

The basis functions in solid angle are defined by the parameterization of planar triangles, since the definition of general functions on spherical triangles is not achievable. If the vertices of a planar triangle are denoted by $\mathbf{r}_1$, $\mathbf{r}_2$, and $\mathbf{r}_3$, each point $\mathbf{r}$ in the planar triangle may be described by the barycentric coordinate system as

$$\mathbf{r} = \begin{pmatrix} x_1 & x_2 & x_3 \\ y_1 & y_2 & y_3 \\ z_1 & z_2 & z_3 \end{pmatrix} \begin{pmatrix} \gamma_1 \\ \gamma_2 \\ \gamma_3 \end{pmatrix} = A\gamma \quad \text{with} \quad \sum_{i=1}^{3} \gamma_i = 1 \tag{33}$$

A point $\mathbf{r}$ on the planar triangle is assigned to a point $\mathbf{s}$ on the spherical triangle by

$$\mathbf{s} = \frac{\mathbf{r}}{|\mathbf{r}|} \tag{34}$$

By inverting Eq. (33) and inserting Eq. (34), $\mathbf{s}$ is represented by a unique parameterization γ_i

$$\gamma = A^{-1}\mathbf{r} = A^{-1}|\mathbf{r}|\mathbf{s} \tag{35}$$

where the distance $|\mathbf{r}|$ of the point on the planar triangle to the origin is unknown. Noting that the planar triangle is part of the plane with the normal form

$$(\mathbf{r} - \mathbf{r}_i) \cdot \mathbf{n} = 0 \rightarrow \mathbf{r} \cdot \mathbf{n} = D = \mathbf{r}_i \cdot \mathbf{n}, \quad i = \{1,2,3\} \tag{36}$$

where $\mathbf{r}_i$ is one of the vertices of the planar triangle and the normal vector is given by

$$\mathbf{n} = (\mathbf{r}_1 - \mathbf{r}_2) \times (\mathbf{r}_1 - \mathbf{r}_3) \tag{37}$$

the norm $|\mathbf{r}|$ is expressed by the points in the spherical triangle by inserting Eq. (34) in Eq. (36)

$$|\mathbf{r}| = \frac{D}{\mathbf{n} \cdot \mathbf{s}} \tag{38}$$

Using this result, Eq. (35) is a function

$$\gamma = \gamma(\mathbf{s}) = A^{-1}\frac{D}{\mathbf{n} \cdot \mathbf{s}}\mathbf{s} \tag{39}$$

of the points on the spherical triangle or the direction $\mathbf{s}$. By using Eq. (39) each basis function

$$\hat{\Phi}^e(\mathbf{r}) = f(\gamma) \tag{40}$$

defined on the planar triangle may be used as basis function

$$\Phi^e(\mathbf{s}) = f(\gamma(\mathbf{s})) \tag{41}$$

of the direction $\mathbf{s}$.

By noting that the restriction

$$\sum_{i=1}^{3} \gamma_i = 1 \tag{42}$$

in Eq. (33) requires $\gamma_3 = 1 - \gamma_1 - \gamma_2$, it is obvious that the inverse of Eq. (33) directly defines the commonly used linear basis function on the planar triangle and, hence, Eq. (39) defines the equivalent linear function on the spherical triangle.

3 Results and Discussion

Based on the theoretical and analytical considerations described previously, computer codes have been developed that are able to simulate one-dimensional, two-dimensional, and three-dimensional RHT problems. While the one-dimensional code is implemented using the MATLAB [24] environment, the multidimensional codes are implemented in the C programming language. For the results to be discussed subsequently, linear basis functions in the spatial domain and linear basis functions in the angular domain were used as defined by Eq. (39). The angular discretizations were obtained from different stages of refinement of the octahedron and are labeled as "SAFE M_Ω," where M_Ω is the number of nodes of the mesh in the total solid angle as given by Eq. (32) and SAFE is an acronym for solid angle finite element. The coefficients of the angular linear system Eq. (18) were calculated by numerical integration, where each spherical triangle is subdivided in a number of smaller triangles and a Newton–Cotes quadrature is employed in the subtriangles. A criterion for the accuracy of the integration was the total sum of the distinct coefficients, which must conform to the analytical values of the well-known angular moments [23]. Solutions of the linear system of equations were calculated by the stabilized conjugate gradient method from van der Vorst [25]. To compare the proposed method to well-established methods, computer codes based on the same spatial finite element code using the EP-DOM [26] together with the level symmetric hybrid (LSH)-quadratures [27], and the P_1-approximation [28] with Marshak's boundary conditions were developed.

In order to assess the performance of the method, benchmarks were computed and compared with the exact solution. These benchmarks are commonly used to analyze the performance of a computational solution technique for the RTE [16,22]. In all cases the incident radiation, Eq. (27), and the radiative heat flux, Eq. (28), were calculated. For the assessment of the accuracy the errors are quantified by the root mean square (rms) defined as

$$\mathrm{rms}(y) = \sqrt{\frac{1}{N}\sum_{i}^{N} (y(z_i) - y^{\mathrm{exact}}(z_i))^2} \tag{43}$$

In the following, test cases with highly simplified geometries were investigated, for which analytical solutions are available. The application of the method to more realistic three-dimensional geometries has been reported recently [15].

3.1 Test Case A: Emitting and Absorbing Plane-Parallel Medium. An emitting and absorbing plane-parallel medium with prescribed temperature bounded by black, cold walls was investigated as a first test case. This problem is attractive since the analytical solution is easily calculated to arbitrary precision, and it allows to obtain a first impression of the fundamental quality of the approximation method.

In Figs. 3 and 4 the net heat flux q and the incident radiation G are plotted as calculated by the finite element method for optical thicknesses $\kappa L = 0.1$, 1.0, and 10.0. In each case, the temperature of the medium was equivalent to $I_b = 1/\pi$. Because of the symmetry of the problem, the figures show only 1/2 of the solution domain. The analytical solutions are calculated from the equations given in the textbook by Modest [28].

While the finite element method predicts the net radiative heat flux with good accuracy for all stages of refinement of the angular mesh and optical thicknesses κL, the predicted incident radiation

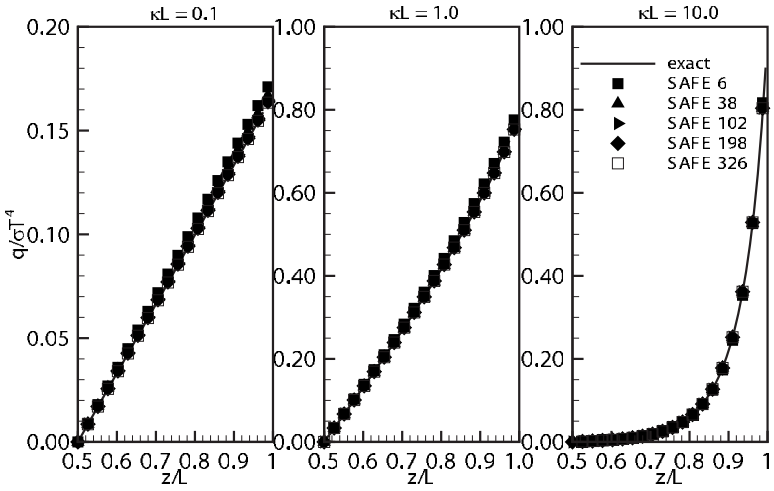

Fig. 3 Test case A: Radiative heat flux q in an emitting-absorbing plane-parallel medium

in the optically thin case differs significantly from the analytical results for coarser angular grids. A detailed insight in the prediction quality of the SAFE in dependence of the angular and spatial mesh is given by Figs. 5 and 6. The reason for the error trends as displayed by these figures is easily understood by the inspection of Fig. 7.

Independent of the optical thickness the intensity in directions parallel to the walls is $I(z,0)=I_b$. In the optically thick case approximately the same intensity is obtained independent of the direction for locations far enough from the walls. Approaching the cold walls, the intensity in either the upper or the lower hemisphere will drop rapidly to zero. From this observation the values for Ψ in the EP equation may be deduced. With Eq. (4) and the symmetry properties of Ψ, the value $\Psi(z)=2/\pi$ can be derived for all directions in the symmetry plane $z=L/2$. Using again Eq. (4), the direction independent value $\Psi(z,\mu)=1/\pi$, for $\mu\neq 0$, can be derived for positions in the vicinity of the walls. A directional dependence of Ψ can only be observed at positions between the symmetry plane and the wall. There, Ψ decreases smoothly from $2/\pi$ to $1/\pi$ for directions perpendicular to the wall, while $\Psi(z,\mu)$ for directions nearly parallel to the wall displays a steep gradient in the close vicinity to the boundary. Summarizing these considerations, it can be concluded that in the optically thick case a moderate number of angular nodes is sufficient, but a small spatial element size is necessary. This conclusion is confirmed by the rms values calculated from the predicted net heat fluxes and incident radiation as depicted in Figs. 5 and 6. It is obvious that the lowest-order angular discretization does not yield a satisfactory accuracy and the rms rapidly converges toward a limit when refining the spatial grid. As expected, the refinement of the spatial grid has a strong major influence on the accuracy of the solution, provided the angular discretization is fine enough.

The opposed characteristics can be found for the optically thin case. In the symmetry plane the intensity normal to the walls is $I(z,\pm 1)\approx(\kappa L I_b)/2$. It increases for $\mu\rightarrow 0$ exponentially toward the limit $I(z,0)=I_b$. When approaching the upper wall, the intensity $I(z,0)$ remains constant and $I(L,1)$ is twice the value in the symmetry plane. According to Eq. (4) and the symmetry properties of Ψ, this implies that $\Psi(z,\mu)$ is nearly independent of the position inside the medium and decreases only for directions near $\mu=0$ approximately to the half. Therefore, the spatial element size plays a less significant role. These assumptions are confirmed by the results of the finite element calculations presented in Fig. 4. Clearly, the finite element approximation is not capable of predicting the incident radiation with an error less than 40% in the case of a coarse angular mesh. Only with the refinement of the angular grid satisfactory predictions can be obtained. This is verified by the results plotted in Figs. 5 and 6. Obviously, an improvement of

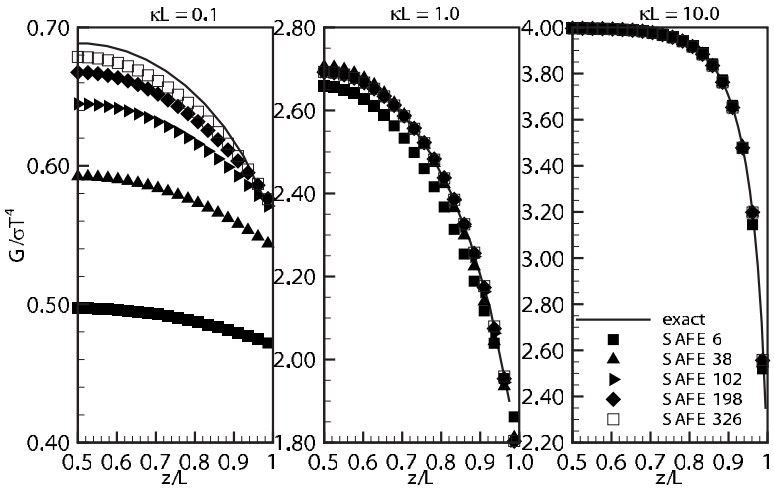

Fig. 4 Test case A: Incident radiation G in an emitting and absorbing parallel medium

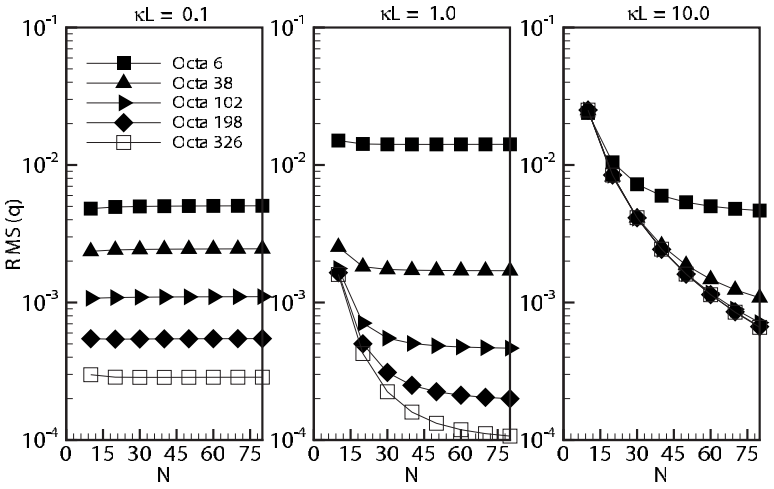

Fig. 5 Test case A: rms values of net heat flux predictions

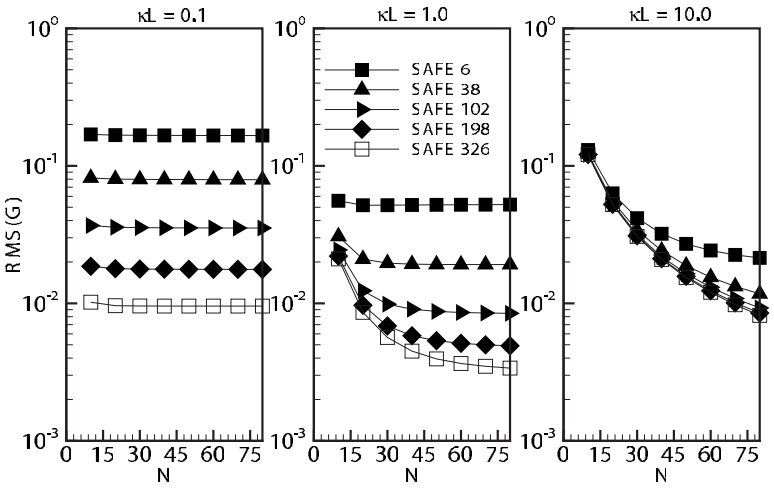

Fig. 6 Test case A: rms values of incident radiation predictions

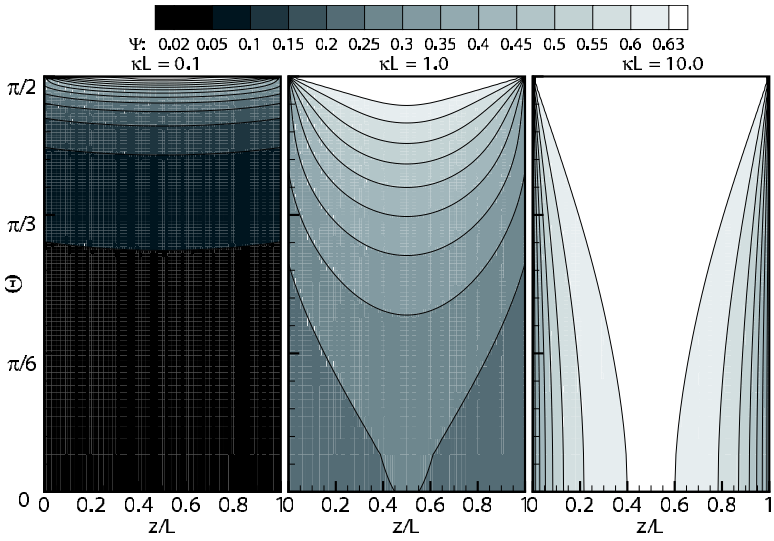

Fig. 7 Contour plots of the exact solution of the even-parity equation

Table 1 rms of the net heat flux and the incident radiation in case of the emitting-absorbing one-dimensional media. The CPU times for the solution of the linear systems is also given.

	κ	SAFE 6	SAFE 38	SAFE 102	SAFE 198	S_4	S_6	S_8	S_{10}	P_1
rms(q)	0.1	0.00502	0.00244	0.00110	0.00054	0.00538	0.00349	0.00280	0.00235	0.00838
	1.0	0.01412	0.00172	0.00050	0.00025	0.00468	0.00741	0.00577	0.00427	0.07325
	10.0	0.00598	0.00260	0.00243	0.00244	0.00724	0.00206	0.00173	0.00175	0.02532
rms(G)	0.1	0.16658	0.07959	0.03544	0.01772	0.17956	0.11548	0.09233	0.07746	0.28245
	1.0	0.05192	0.01929	0.00906	0.00581	0.04322	0.03972	0.03185	0.02544	0.23916
	10.0	0.03208	0.02420	0.02184	0.02115	0.03780	0.02808	0.02573	0.02451	0.05922
CPU time (s)	0.1	0.05300	0.53264	5.01022	5.88745	0.05244	0.08104	0.10606	0.13590	0.01463
	1.0	0.08041	0.34273	0.78240	1.73669	0.04869	0.08678	0.10012	0.16603	0.01506
	10.0	0.02777	0.06405	0.13680	0.24494	0.04613	0.06248	0.08591	0.11616	0.01794

the quality of the prediction is only possible with refinement of the angular mesh and an influence of the spatial grid size is not observed.

3.1.1 Comparison to the DOM and the P_1-Approximation. For comparison of the finite element method with the well-established DOM and P_1-approximation the same test case was calculated using these methods. The rms values obtained from these approximations are tabulated in Table 1, together with the results obtained from the SAFE method. Comparison of the rms reveals that the SAFE outperforms the DOM for all angular discretizations. In the optically thin case, $\kappa L=0.1$, and the optical intermediate case, $\kappa L=1.0$, the SAFE 38 with 38 angular nodes predicts the heat flux and the incident radiation with comparable accuracy to the DOM with the S_{10} quadrature (120 nodes). A very different behavior is found in the optically thick case. Here, the two coarsest angular grids predict the radiative heat flux with an accuracy comparable to the S_4 and S_6 DOM. If angular meshes with more nodes are used, the rms reaches a limiting value (see Fig. 5) and the results obtained with the DOM simulations are of higher quality than those calculated by the finite element method. The rms values of the incident radiation as calculated by the finite element method are always lower than the rms values calculated by the DOM.

The effect of the optical thickness on the accuracy of the SAFE, the DOM, and the P_1 was investigated from the calculations as presented in Fig. 8. In this figure the rms is plotted versus the optical thickness for two spatial discretizations. It can be seen that the SAFE ensures better results than the two other angular discretization methods provided the spatial grid is fine enough. If not, the prediction error increases linearly with increasing optical thickness. The same behavior is found for the DOM, but with the DOM the increase in the error starts at larger optical thicknesses as compared with the finite element method.

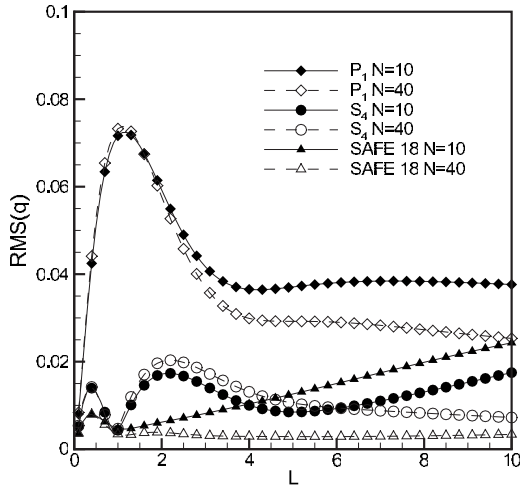

Fig. 8 Test case A: Comparison of the rms(q) calculated with the finite element method, the DOM, and the P_1-approximation

A second criterion besides accuracy is computational time needed by a solution method. Table 4 tabulates the CPU time required for the solution of the linear systems resulting from the DOM, the P_1, and the SAFE. For absorbing and emitting media the SAFE needs, in general, more CPU time in optically thin cases than in optically thick cases. This is not surprising since the FEM for parabolic second-order equations gives rise to coefficient matrices with a condition number inversely proportional to the square of the effective mesh width. Furthermore, the typical convergence rates of conjugate gradient methods are proportional to the root of the condition number [21]. Summarizing this, convergence rates directly proportional to the inverse of the optical thickness can be expected. Compared with the DOM, the SAFE method needs notably larger computational resources in the thinner media. Here the low convergence rate combined with the larger number of unknowns strongly increases runtime. In the optically thick case, the CPU times of the DOM and the SAFE are of comparable order. However, it should be remembered that in all cases the SAFE provides better accuracy than the DOM at a given number of angular nodes; hence, runtime increase may be less significant.

3.2 Test Case B: Isotropically Scattering, Nonabsorbing Plane-Parallel Medium. In this test case the RHT in a nonabsorbing, isotropically scattering medium was considered. The wall at $z=0$ was held at a temperature equivalent to the blackbody intensity $I_b=1/\pi$ and the wall at $z=L$ was assumed black and cold. The test case was calculated for three optical thicknesses, $\sigma L=0.2$, 1.0, and 2.0. Since the medium is gray, this problem is physically equivalent to radiative equilibrium where the divergence of the radiative heat flux is zero. Highly accurate solutions for this test case are available from the studies of Heaslet and Warming [29,30].

Again, the test cases were calculated with multiple subdivisions of the octahedron. The predicted net heat fluxes and incident radiation are tabulated in Table 2 and depicted in Fig. 9, respectively. Because of the symmetry of the problem, Fig. 9 shows only 1/2 of the domain. As in the absorbing and emitting case, the usage of coarser angular grids results in a large error for the optically thin case. In all other cases the predictions of the incident radiation are good. The results in Table 2 indicate that even the angular approximation SAFE 6 with six angular nodes predicts the net heat flux within a deviation of 0.9–0.4% from the expected values depending on the optical thickness. The results of all other angular discretizations are much closer to the analytical results. Again, the rms of the net heat flux and incident radiation were calculated for the predictions obtained from different angular discretizations and for different refinements of the spatial grid. These rms values are plotted in Fig. 10 for the net heat flux and in Fig. 11 for the incident radiation. Similar to the absorbing-emitting,

Table 2 Predictions for the heat flux from the finite element method, the DOM, and the P_1-approximation

σ	Exact	SAFE 6	SAFE 38	SAFE 102	SAFE 198	S_4	S_6	S_8	S_{10}	P_1
0.2	0.8491	0.8567	0.8502	0.8494	0.8493	0.8406	0.8446	0.8459	0.8467	0.8696
1.0	0.5532	0.5567	0.5540	0.5536	0.5534	0.5416	0.5513	0.5526	0.5529	0.5714
2.0	0.3900	0.3917	0.3904	0.3901	0.3901	0.3836	0.3893	0.3897	0.3898	0.4000

optically thin medium, the error in the case of $\sigma=0.2$ is only a function of the angular mesh size and not of the spatial mesh. A different result is obtained in the optically intermediate and thick cases. Comparing Figs. 10 and 11 it is obvious that the error in the prediction of the incident radiation is more dependent on the spatial mesh than in the prediction of the net heat flux. Starting out from a coarse angular and a coarse spatial mesh, only the refinement of both, the spatial and the angular, grids together improves the accuracy of the calculation of G. However, for all angular discretizations the rms rapidly approaches a limiting value, and further spatial refinement does not enhance the solution quality; though, an anomaly arises for the finest angular grid. First, the refinement of the spatial grid decreases the rms, then a minimum value of the rms is reached and with further refinement, the error increases slightly above the rms values of the next coarser angular grid. The reason for this behavior may be found in the interaction of the errors caused by the spatial and the angular discretizations. The two sources of error seem to balance each other for coarse grids, but with the refinement of the angular and spatial discretizations the compensation effect is reduced.

For comparison of the finite element method with the DOM and the P_1-approximation the heat fluxes computed with these methods are also listed in Table 2. Additionally, the rms values for the predictions obtained by the DOM and the P_1 are tabulated in Table 3. Again, the SAFE method guarantees superior accuracy compared with both other methods. In the optically thin case, the octahedral mesh with 38 angular nodes is capable to achieve better accuracy than the DOM S_{10} with 120 directions. For $\sigma=1.0$ and $\sigma=2.0$ the gap between the methods is smaller, but usage of the SAFE method still ensures a lower rms.

The CPU times needed in this test case are tabulated in Table 4. As observed in the emitting and absorbing medium, the computational time needed by the SAFE decreases with increasing optical

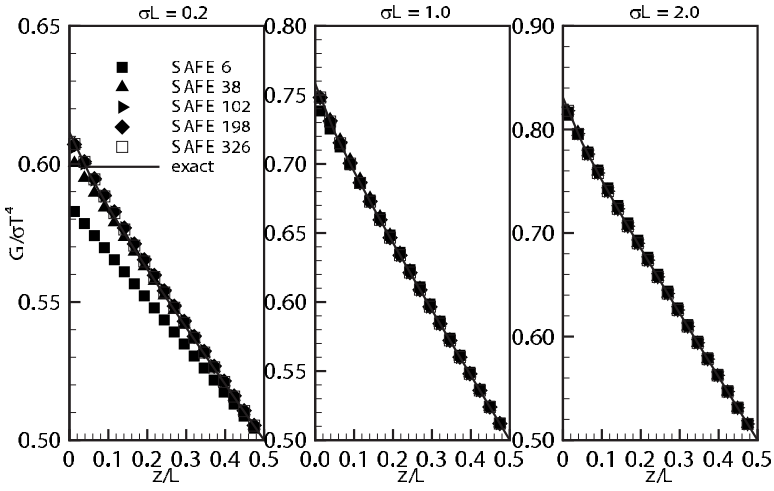

Fig. 9 Test case B: Incident radiation *G*

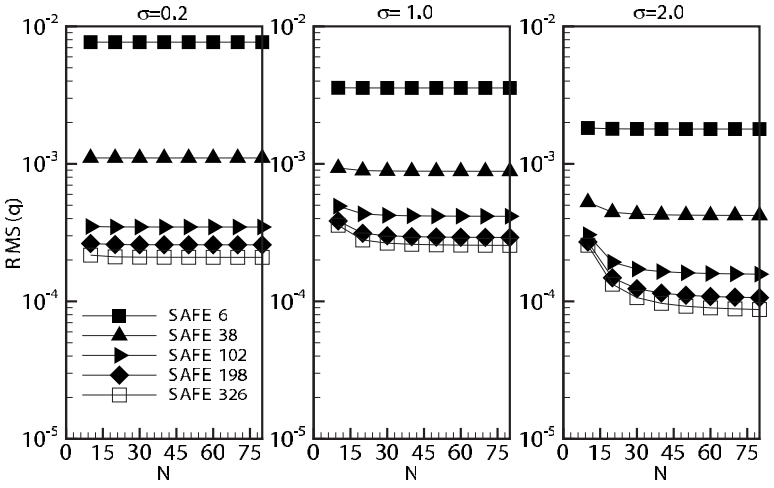

Fig. 10 Test case B: rms values of the net heat flux

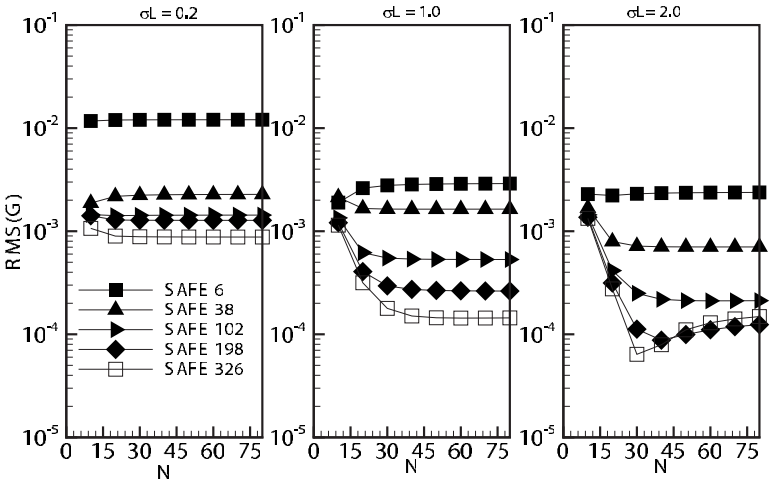

Fig. 11 Test case B: rms values of the incident radiation

thickness. However, compared with the absorbing and emitting media the runtime is increased for angular meshes with a large number of nodes, which is a consequence of the increased number of floating point operations per solver iteration due to the fully occupied angular system in the presence of scattering. In contrast, the runtime of the DOM increases with increasing optical thickness, which is a well-known effect of the outer iteration used in the DOM implementation to update the radiative source term in the RTE [22]. This results in a substantially larger computational effort in the optically intermediate and thick cases compared with the SAFE method.

3.3 Test Case C: Emitting and Absorbing Two-Dimensional Medium. In this section the SAFE method, the EP-DOM, and the P_1-approximation were applied to a two-dimensional, rectangular enclosure with cold, black walls and filled with an absorbing and emitting medium. The medium was maintained at an emissive power of unity everywhere, i.e., the medium is isothermal. The "exact" solution was calculated by a modified exchange factor method. For the approximate methods, the enclosure was discretized with a grid of 20×20 bilinear elements. Calculations were performed for optical thicknesses κL

Table 3 rms of the net heat flux and the incident radiation in case of the isotropically scattering one-dimensional media. The CPU times for the solution of the linear systems are also given.

	σ	SAFE 6	SAFE 38	SAFE 102	SAFE 198	S_4	S_6	S_8	S_{10}	P_1
rms(q)	0.2	0.00768	0.00110	0.00035	0.00026	0.00847	0.00445	0.00318	0.00244	0.02047
	1.0	0.00357	0.00089	0.00042	0.00030	0.01160	0.00192	0.00065	0.00034	0.01823
	2.0	0.00179	0.00043	0.00016	0.00011	0.00646	0.00070	0.00029	0.00024	0.01000
rms(G)	0.2	0.01205	0.00226	0.00143	0.00128	0.00348	0.00185	0.00258	0.00290	0.02338
	1.0	0.00284	0.00164	0.00054	0.00027	0.00814	0.00387	0.00233	0.00161	0.01742
	2.0	0.00234	0.00071	0.00022	0.00009	0.00532	0.00139	0.00104	0.00081	0.00924
CPU time (s)	0.2	0.07417	0.40852	1.61102	5.41748	0.48638	0.79392	1.06637	1.32141	0.02629
	1.0	0.07076	0.23242	0.70655	1.89832	1.34552	1.99621	2.64747	3.33634	0.02545
	2.0	0.06998	0.17427	0.49531	1.26530	2.47727	3.48432	4.73401	5.79145	0.02327

Table 4 rms of the net heat flux and the incident radiation in case of an emitting-absorbing and an isotropically scattering two-dimensional medium. The CPU times for the solution of the linear systems are also given.

Test case C	βL	SAFE 18	SAFE 38	SAFE 66	SAFE 102	S_4	S_6	S_8	P_1
rms(q)	0.1	0.00963	0.00499	0.00664	0.00686	0.01088	0.00965	0.00805	0.02158
	1.0	0.03819	0.01858	0.01922	0.02433	0.05286	0.02238	0.02756	0.12401
	10.0	0.09804	0.11488	0.12252	0.12594	0.10186	0.10607	0.10899	0.08331
rms(G)	0.1	0.08116	0.03071	0.02834	0.04319	0.01644	0.02457	0.03724	0.26145
	1.0	0.17569	0.06889	0.02429	0.02030	0.13579	0.03982	0.09387	0.67349
	10.0	0.03412	0.02728	0.02453	0.02449	0.06440	0.03444	0.02012	0.12955
CPU times (s)	0.1	2.297	5.713	11.280	17.136	1.150	2.457	4.500	0.041
	1.0	0.740	1.939	3.533	5.704	0.885	1.751	3.025	0.038
	10.0	0.523	1.017	2.439	3.709	0.619	1.289	2.145	0.037
Test case D									
rms(q)	1.0	0.07181	0.03732	0.02665	0.02234	0.14479	0.06472	0.04343	0.01377
rms(G)	1.0	0.18534	0.12030	0.11223	0.10978	0.25752	0.09945	0.11552	0.28216
CPU times (s)	1.0	0.593	2.476	7.115	18.264	4.874	9.091	17.073	0.041

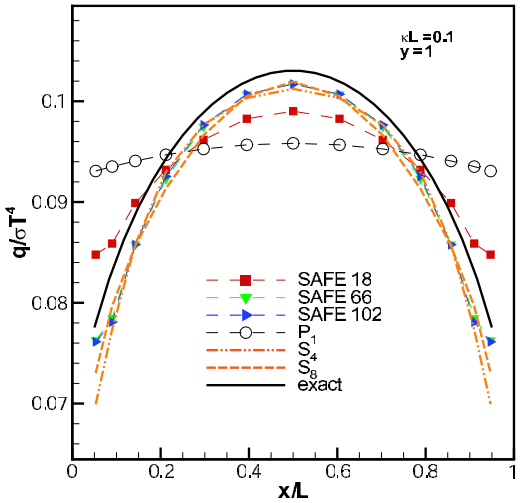

Fig. 12 Test case C: Radiative heat flux profiles at the walls of an emitting and absorbing two-dimensional medium

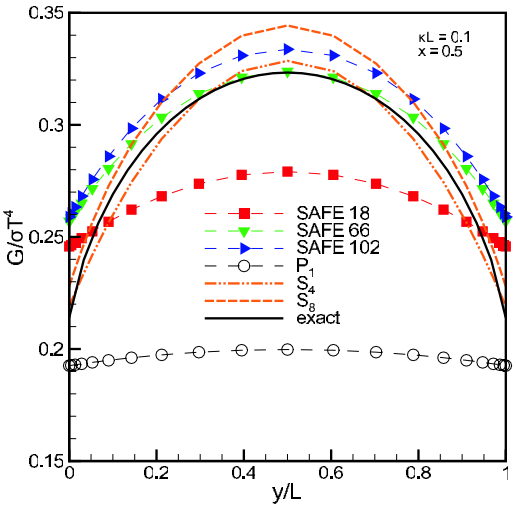

Fig. 14 Test case C: Incident radiative intensity in the centerline of an emitting and absorbing two-dimensional medium

=0.1, κL=1.0, and κL=10.0.

Figures 12 and 13 show the radiative heat fluxes at the top of the two-dimensional enclosure for an optical thickness κL=0.1 and κL=1.0, respectively. The incident radiation at the centerline y=0.5 is presented in Figs. 14 and 15. In both cases the finite element solutions are able to predict the expected heat flux q and incident radiation G with satisfactory accuracy. As in the one-dimensional case the incident radiation calculated from SAFE with coarse angular grids differs considerably from the exact values in the optically thin medium. The reason for this deviation may be directly understood from the discussion for the one-dimensional case. As pointed out there, the intensity in optically thin media is strongly dependent on direction. Hence, increased coupling between different directions in a low-order approximation has a negative influence on the accuracy. This fact is clearly confirmed by comparison of the results of the SAFE with the results obtained from the P_1-approximation and the DOM, as depicted in Fig. 14. While the SAFE 18 and the P_1 cannot reproduce the profile of the incident radiation, the S_4 DOM represents the expected distribution fairly well. Furthermore, the gradient of the incident radiation nearby the walls is greatly underpredicted by the SAFE and the P_1. This could be due to the Marshak boundary conditions used by both of these methods. In contrast, the DOM, which uses Marshak-like boundary conditions, calculates the incident radiation in the vicinity of the walls much better. Consequently, a comparative study of the boundary conditions applied to the angular finite element method is desired for the future.

The rms values calculated according to Eq. (43) are tabulated in Table 4. Again, the SAFE predicts the heat flux with better accuracy as compared with the two other angular approximation methods considered here. In the case of incident radiation the approximations obtained from the DOM are less error-prone than the results from the angular FEM for optically thin media, as can be expected from the discussion above. In the optically intermediate case, e.g., κL=1.0, the coarser angular meshes SAFE 18 and SAFE 38 perform less well than the S_4 and the S_6 approximations with comparable numbers of angular directions. Nearly always the much simpler P_1-approximation is outperformed by the two other angular approximation methods.

Table 4 lists the CPU times needed for the calculations by the FEM, the DOM, and the P_1. Just as observed for the one-dimensional test cases, the runtime decreases with increasing optical thickness for all methods. Particularly in the optically thin case the CPU usage of the SAFE rises rapidly with the increasing

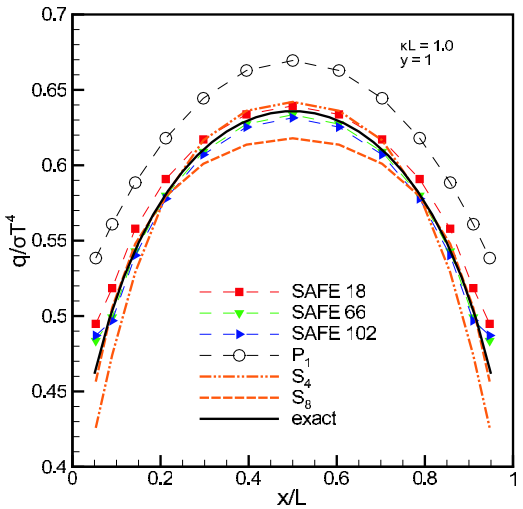

Fig. 13 Test case C: Radiative heat flux profiles at the walls of an emitting and absorbing two-dimensional medium

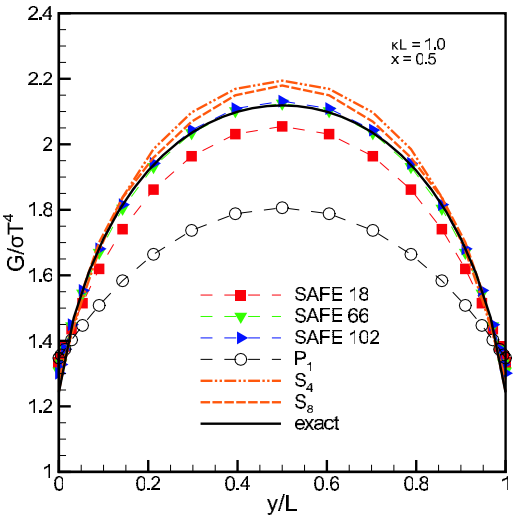

Fig. 15 Test case C: Incident radiative intensity in the centerline of an emitting and absorbing two-dimensional medium

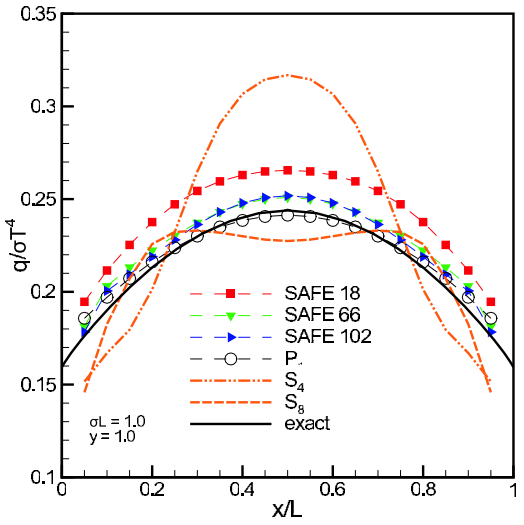

Fig. 16 Test case D: Radiative heat flux at the top of a purely isotropically scattering two-dimensional medium

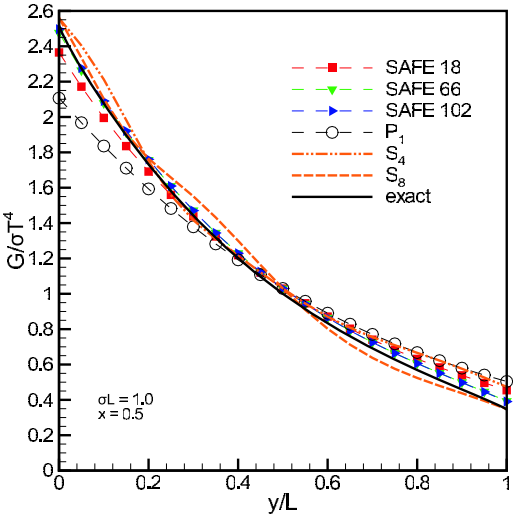

Fig. 17 Test case D: Incident radiative intensity in the center of a purely isotropically scattering two-dimensional medium

number of angular nodes and exceeds the runtime of the DOM. In thicker media the runtime of the SAFE is of the same order as compared with the DOM.

3.4 Test Case D: Purely Isotropically Scattering Two-Dimensional Medium. In this test case the radiative transfer in an isotropically scattering, nonabsorbing two-dimensional medium was considered. The medium was exposed to diffuse irradiation $I=\sigma T^4/\pi$ incident at $y=0$. Since this problem is known to emphasize ray effects [9], it is routinely studied as a benchmark for the DOM. Highly accurate approximations of the radiative heat flux and the source terms for this test case were tabulated by Crosbie and Schenker [31].

Figure 16 shows the net heat flux at the top wall for several SAFE solutions together with the DOM approximations, the P_1, and the results from Crosbie and Schenker [31]. It is clearly visible that the DOM is prone to ray effects in this setup. Hence, the S_4 DOM solution deviates up to 30% from expected values and cannot capture the expected heat flux profile. Using an S_8 quadrature with 80 directions minimizes the ray effect, but does not eliminate it. In contrast, both methods using continuous functions for the approximation of the angular dependence, SAFE and P_1, do not suffer from ray effects. Even the lowest-order SAFE, the SAFE 18 with 18 directions, is capable of predicting the heat flux without any ray effect within a deviation of 7%. By increasing the number of angular nodes the predictions obtained from the finite element approximation approach the exact values. However, the SAFE 102 method does not predict the heat flux closer to the exact values than the SAFE 66 approximation, an effect that has been observed in the one-dimensional case as well. From the results obtained there, it can be concluded that further improvement of the prediction is only available from the refinement of the angular and the spatial grids together.

The incident radiation G on the centerline of the enclosure is depicted in Fig. 17. Again, the DOM is affected by the ray effect, independent of the angular quadrature used. As observed in the predictions of the radiative heat flux no ray effect occurs in the angular finite element method and the P_1-approximation. However, the finite element method calculates the incident radiation with a smaller error nearby the walls than the P_1.

4 Conclusion

In the present paper a new and promising solution technique is presented for the radiative heat transfer equation. Starting out from the even-parity formulation, a finite element discretization is applied to the angular and the spatial domains. The mathematical formulation of the angular discretization is general in the sense that nearly arbitrary angular basis functions may be used. In the present work, the angular dependence was treated by a series expansion of piecewise linear basis functions defined on subdivisions of an octahedron. This approach enables a sound derivation of angular approximations with high order. For the assessment of the solution capabilities the convergence characteristics of the spatial and the angular refinement were inspected in one-dimensional test cases. These tests revealed the high accuracy of the present method compared with the commonly used discrete ordinate method and the P_1-approximation. The application of the proposed method to two-dimensional test cases demonstrated the advantageous attributes in higher dimensional calculations as well. Unfavorable may be the somewhat larger runtime of the new method, particularly in optically thin media. Most notably is the ability of the new method to avoid ray effects efficiently, as was demonstrated in a two-dimensional medium exposed to diffuse radiation.

Even though the method was presented and formulated here only for gray media, the incorporation of typical spectral models is straightforward.

Acknowledgment

Thanks are due to Prof. Sigmar Wittig, who initiated the research on radiative transfer in the institute and to the state of Baden-Württemberg, which supported the research through the TECFLAM cooperation. During his research visit at the Universität Karlsruhe, M.F.M. was financially supported by the research award of the Alexander von Humboldt Stiftung, Germany.

Nomenclature

A_{nmpq} = matrix element of a linear system
b_{np} = element of a source vector
E_b = blackbody emissive power (W m^{-2})
E_n = exponential integral of order n
f = arbitrary function
G = incident radiation (W m^{-2})
I = radiative intensity (W m^{-2} sr^{-1})
I_b = blackbody radiative intensity (W m^{-2} sr^{-1})
L = length (m)
m = index
M_Ω = number of angular basis functions
M_r = number of spatial basis functions

n = index
N = number of samples
$\mathbf{n}$ = unit surface normal
p = index
q = index
$\mathbf{q}, q$ = radiative heat flux (W m^{-2})
$\mathbf{r}$ = position vector (m)
$\mathbf{r}_i$ = position vector of node i (m)
$\mathbf{s}$ = unit vector into a direction
T = temperature (K)
V = volume (m^3)
W = weight function
z = Cartesian coordinate (m)

Greek

β = extinction coefficient (m^{-1})
γ_i = barycentric coordinate
κ = absorption coefficient (m^{-1})
η = direction cosine
Ψ = even-order intensity (W m^{-2} sr^{-1})
μ = direction cosine
ξ = direction cosine
σ = scattering coefficient (m^{-1})
σ = Stefan–Boltzmann constant 5.670×10^{-8} W m^{-2} K^{-4}
Φ_n = nth angular basis function
$\hat{\Phi}_n$ = nth spatial basis function
Λ = odd-order intensity (W m^{-2} sr^{-1})
ω_n^{ij} = coefficient (angular linear system) (sr)
$\bar{\omega}_n$ = coefficient (angular linear system) (sr)
Ω = solid angle (sr)
Ω_{nm}^{ij} = coefficient (angular linear system) (sr)
$\bar{\Omega}_{nm}$ = coefficient (angular linear system) (sr)

References

[1] Viskanta, R., and Mengüç, M. P., 1987, "Radiation Heat Transfer in Combustion Systems," Prog. Energy Combust. Sci., **13**(2), pp. 97–160.
[2] Mishra, S. C., and Prasad, M., 1998, "Radiative Heat Transfer in Participating Media—A Review," Sadhana: Proc., Indian Acad. Sci., **23**(2), pp. 213–232.
[3] Viskanta, R., 2008, "Computation of Radiative Transfer in Combustion Systems," Int. J. Numer. Methods Heat Fluid Flow, **18**(3/4), pp. 415–442.
[4] Chandrasekhar, S., 1960, *Radiative Transfer*, Dover, New York.
[5] Davison, B., 1958, *Neutron Transport Theory*, Clarendon, Oxford.
[6] Lathrop, K. D., 1968, "Ray Effects in Discrete Ordinates Equations," Nucl. Sci. Eng., **32**, pp. 357–369.
[7] Raithby, G. D., and Chui, E. H., 1990, "A Finite-Volume Method for Predicting a Radiant Heat Transfer in Enclosures With Participating Media," ASME J. Heat Transfer, **112**, pp. 415–423.
[8] Chai, J. C., Lee, H. S., and Patankar, S. V., 1994, "Finite Volume Method for Radiation Heat Transfer," J. Thermophys. Heat Transfer, **8**(3), pp. 419–425.
[9] Ramankutty, M. A., and Crosbie, A. L., 1997, "Modified Discrete Ordinates Solution of Radiative Transfer in Two-Dimensional Rectangular Enclosures," J. Quant. Spectrosc. Radiat. Transf., **57**(1), pp. 107–140.
[10] Gradstejn, I. S., and Ryzik, I. M., 2007, *Table of Integrals, Series, and Products*, 7th ed., Academic, New York.
[11] Modest, M., and Yang, J., 2008, "Elliptic PDE Formulation and Boundary Conditions of the Spherical Harmonics Method of Arbitrary Order for General Three-Dimensional Geometries," J. Quant. Spectrosc. Radiat. Transf., **109**(9), pp. 1641–1666.
[12] Song, T.-H., and Park, C. W., 1992, "Formulation and Application of the Second-Order Discrete Ordinate Method," *Transport Phenomena and Science*, B.-X. Wang, ed., Higher Education, Beijing, pp. 833–841.
[13] Ohnishi, T., 1972, "Finite-Element Solution Techniques for Neutron-Transport Equations," *Proceedings of the Conference on Numerical Reactor Calculations*, Int. Atomic Energy Agency, pp. 629–638.
[14] Briggs, L. L., Miller, W. F., and Lewis, E. E., 1975, "Ray-Effect Mitigation in Discrete Ordinate-Like Angular Finite Element Approximations in Neutron-Transport," Nucl. Sci. Eng., **57**, pp. 205–217.
[15] Becker, R., Koch, R., and Bauer, H.-J., 2007, "Solution of the Radiative Transfer Equation by a Finite Element Discretization of the Solid Angle," *Proceedings of the Fifth International Symposium on Radiative Transfer*, ICHMT.
[16] Coelho, P., 2005, "Fundamentals of a New Method for the Solution of the Radiative Transfer Equation," Int. J. Therm. Sci., **44**, pp. 809–821.
[17] Pontaza, J., and Reddy, J., 2005, "Least-Squares Finite Element Formulations for One-Dimensional Radiative Transfer," J. Quant. Spectrosc. Radiat. Transf., **95**, pp. 387–406.
[18] Cui, X., and Li, B. Q., 2005, "A Mixed-Mesh and New Angular Space Discretization Scheme of Discontinuous Finite Element Method for Three-Dimensional Radiative Transfer in Participating Media," ASME J. Heat Transfer, **127**, pp. 1236–1244.
[19] Widmer, G., and Hiptmair, R., 2007, "Sparse Finite Elements for Non-Scattering Radiative Transfer in Diffuse Regimes," *Proceedings of the Fifth International Symposium on Radiative Transfer*, ICHMT.
[20] Lewis, E. E., and Miller, W. F., 1984, *Computational Methods of Neutron Transport*, Wiley Interscience, New York.
[21] Eriksson, K., Estep, D., Hansho, P., and Johnson, C., 1996, *Computational Differential Equations*, Cambridge University Press, Cambridge, England.
[22] Fiveland, W. A., and Jessee, J. P., 1994, "Finite-Element Formulation of the Discrete-Ordinate Method for Multidimensional Geometries," J. Thermophys. Heat Transfer, **8**(3), pp. 426–433.
[23] Koch, R., and Becker, R., 2004, "Evaluation of Quadrature Schemes for the Discrete Ordinate Method," J. Quant. Spectrosc. Radiat. Transf., **84**(4), pp. 423–435.
[24] MathWorks Inc., 2006, "MATLAB—The Language of Technical Computing."
[25] van der Vorst, H. A., 1992, "Bi-CGSTAB: A Fast and Smoothly Converging Variant of Bi-CG for the Solution of Nonsymmetric Linear Systems," SIAM (Soc. Ind. Appl. Math.) J. Sci. Stat. Comput., **13**, pp. 631–644.
[26] Koch, R., Krebs, W., Wittig, S., and Viskanta, R., 1995, "A Parabolic Formulation of the Discrete Ordinates Method for the Treatment Of Complex Geometries," *Proceedings of the First International Symposium on Radiative Transfer*, M. P. Mengüç, ed., ICHMT, Begell House, Redding, CT, pp. 43–61.
[27] Fiveland, W. A., 1991, "The Selection of Discrete Ordinate Quadrature Sets for Anisotropic Scattering," *Fundamentals of Radiation Heat Transfer*, W. A. Fiveland, A. L. Crosbie, A. M. Smith, and T. F. Smith, eds., ASME, New York, **HTD-160**, pp. 89–96.
[28] Modest, M. F., 2003, *Radiative Heat Transfer*, 2nd ed., Academic, New York.
[29] Heaslet, M. A., and Warming, R. F., 1965, "Radiative Transport and Wall Temperature Slip in an Absorbing Planar Medium," Int. J. Heat Mass Transfer, **8**, pp. 979–994.
[30] Heaslet, M. A., and Warming, R. F., 1967, "Radiative Transfer in an Absorbing Planar Medium II—Predictions of Radiative Source Functions," Int. J. Heat Mass Transfer, **10**, pp. 1413–1427.
[31] Crosbie, A. L., and Schenker, R. G., 1984, "Radiative Transfer in a Two-Dimensional Rectangular Medium Exposed to Diffuse Radiation," J. Quant. Spectrosc. Radiat. Transf., **31**(4), pp. 339–372.